

HYDROGEN AND HELIUM SHOCK PHENOMENA DURING RISING LIGHT IN RR LYRAE FUNDAMENTAL MODE PULSATORS

GEORGE W. PRESTON,¹ CHRISTOPHER SNEDEN,² AND MERIEME CHADID³

¹*Carnegie Observatories, 813 Santa Barbara Street, Pasadena, CA 91101, USA; gwp,ian,shc@obs.carnegiescience.edu*

²*Department of Astronomy and McDonald Observatory, The University of Texas, Austin, TX 78712, USA; chris@verdi.as.utexas.edu*

³*University of Côte d’Azur, Nice Sophia–Antipolis University, CNRS–UMR 7250, CS 34229, 06304 NICE Cedex 4, France; chadid@unice.fr*

ABSTRACT

We present measurements of H and He emission and absorption lines produced in R Rab fundamental mode pulsators during primary light rise. The lines define universal progressions of rise and decay in metal-poor R Rab stars. Such a progression cannot be constructed for He in metal-rich R Rab (those with $[\text{Fe}/\text{H}] > -0.8$) because weak He I emission is detected in only two of the six metal-rich R Rab in our survey. Great variety exists in the phase variations of the blue- and red-shifted absorption components of the 5876 Å line during pre- and post-emission phases. Detection of measurable He II 4686 Å emission in eight R Rab, three of them Blazhko variables, provides an additional constraint on ionization of Helium.

1. INTRODUCTION

Two weakly-visible H α emission episodes attributed to shock phenomena occur in R Rab stars during declining light. The first, dubbed the “third apparition” (Preston 2011), is identified by a weak red-shifted H α emission wing visible during about one third of the pulsation cycle following maximum light. Ad hoc explanations of this apparition have been advanced by Chadid & Preston (2013) and Gillet et al. (2017, 2019). A second shock, identified by violet-shifted H α emission during the “bump” preceding minimum light (Gillet & Crowe 1988), is discussed at length in the foregoing references. The existence of this shock was anticipated theoretically by the calculations of Hill (1972). Both emissions are accompanied by absorption line-doubling produced in outflowing and infalling atmospheric layers.

Chadid et al. (2014) detected multi-shocks propagating through the atmosphere of RR Lyrae stars. They identified new light curve properties¹ induced by five shock waves, with different amplitudes and origins. Recently Prudil et al. (2020) have used broad band photometry to identify (hump) shock phenomena in a large sample of field R Rab. Metallic-line absorption phenomena, particularly shock-induced increases in macroturbulence during rising in stable R Rab, were reviewed by Preston (2009), and studied in great detail more recently by Preston et al. (2019).

Corresponding author: Christopher Sneden
chris@verdi.as.utexas.edu

¹ nicknamed *jump*, *lump*, *rump*, *bump*, and *hump*, as introduced by Christy 1966 and expanded by Chadid et al. 2014

This paper deals with strong shock phenomena (“first apparition”, the hump) during primary light-rise, discovered spectroscopically by Sanford (1949) and interpreted soon thereafter by Schwarzschild (1952). All previous discussions of this primary shock in RR Lyrae stars have been based solely on the behaviors of Balmer emission and absorption lines in the context of the Schwarzschild model. Wallerstein (1959) explored shock conditions in the Pop II Cepheid W Virginis. He calculated, by taking into account the energy of ionization in application of the Rankine-Hugoniot relations, that a shock velocity higher than 80 km s^{-1} is able to ionize Hydrogen and neutral Helium and, additionally, a small fraction of singly-ionized Helium. This condition is fulfilled by typical RRab stars (to be discussed in §3.1.3), so it came as no great surprise that Preston (2009, 2011) detected He I emission and absorption lines during light-rise in 10 RRab stars and very weak He II 4685.68 \AA emission in 3 RRab stars. These H and He emissions, produced in the wakes of shock waves, can provide quantitative insight into the stratification of the outflowing and infalling atmospheric layers.

In this paper we present new information about the time evolution of the pulsation velocities, equivalent widths, and line-of-sight broadening of the emission and absorption of the most prominent lines of H, He I and He II in our spectra. The format of the paper is as follows. In §2 we describe the data set; in §3 we present Hydrogen and Helium emission and absorption line measurements; and in §4 we discuss issues raised by the behavior of the He I $\lambda 5876$ line. §5 contains our concluding remarks.

2. THE SPECTROSCOPIC DATA SET

2.1. Observations and Reductions

For this study we mine the database of several thousand echelle spectra of RR Lyrae stars that were obtained with the du Pont 2.5 m telescope at Las Campanas Observatory between 2006 and 2014. The resolving power of these spectra is $R \equiv \lambda/\delta\lambda = 27,000$ at 5000 \AA . We concentrate on a subset of stars analyzed by Chadid et al. (2017) that have many spectra in the phase range $\phi = 0.8\text{--}1.1$. In Table 1 we list the observed photometric pulsational properties and metallicities of the RR Lyraes considered in the present work. The pulsational data are taken from Chadid et al. Table 1. The adopted metallicities are means of the [Fe I/H] and [Fe II/H] values (with assumed $\log \epsilon(\text{Fe})_{\odot} = 7.50$) listed in Table 2 of that paper.

RR Lyrae stars pulsate with periods mostly confined to the range $0.25 \text{ d} < P < 0.75 \text{ d}$. Target exposure times, limited to small fractions of these periods, never exceeded 600 s ($\sim 0.01P$), which resulted in relatively poor signal-to-noise ratios in the blue spectral region, $S/N \sim 15\text{--}20$ for most of the stars in our sample. This created challenges for derivation of photospheric quantities (T_{eff} , $\log g$, V_{mic} , [Fe/H] metallicity, [X/Fe] abundance ratios) from these spectra, because the great majority of detectable metallic lines in RR Lyrae stars occur at wavelengths less than 5000 \AA . On the other hand, the H and He transitions used in this investigation lie in the yellow and red region, $\lambda > 5000 \text{ \AA}$, where our spectra have much higher $S/N \sim 50\text{--}80$.

The du Pont echelle observations were reduced to final spectra as described in detail by For et al. (2011a). These spectra have been used in multiple papers since that time. Therefore the reduction procedures will not be repeated here. The individual du Pont multi-order wavelength calibrated

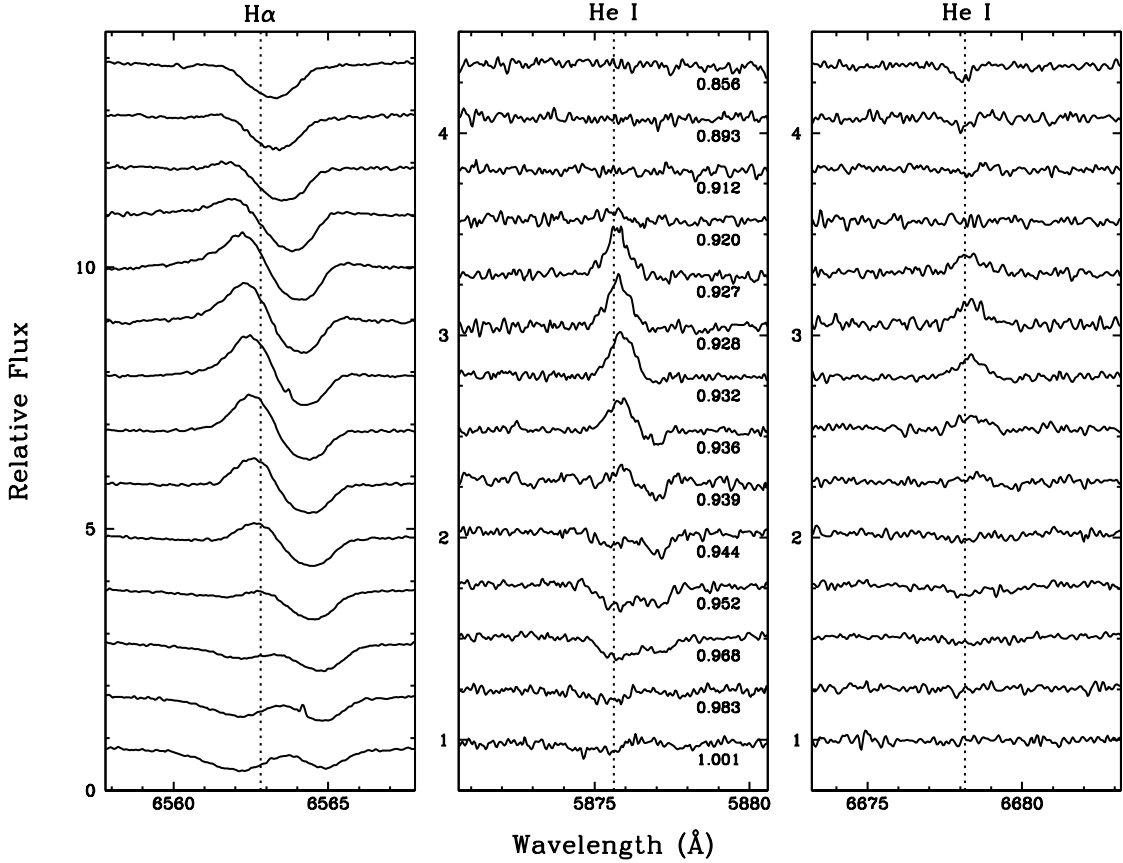


Figure 1. Variations of $H\alpha$, He I 5875.62 Å, and He I 6678.15 Å, in the rising light shock phases of RV Oct. Dotted lines indicate the rest wavelengths of these lines as defined by the metallic lines. The phases are written in the middle panel.

spectra of all stars that we obtained in the 2006-2014 time period, whether or not they have been used in the present paper, can be obtained at the Zenodo data depository²

2.2. The Transitions

In Figure 1 we extend Figure 1 of Preston (2009) by showing the variation with phase near maximum light of RV Oct for $H\alpha$ and the two He I lines with strongest emission, 5875.62 Å and 6678.15 Å. The rapid appearance and fadeout of He I emission lines are illustrated in the sequence of RV Oct spectra in the phase range $0.66 \lesssim \phi \lesssim 1.00$. Discussion of detailed $H\alpha$ phase variations has been included in previous papers in this series for RRab stars (Chadid et al. 2017) and for RRC (Snedden et al. 2017). For RV Oct the He I emission occurs only in the narrow phase range $\phi = 0.92-0.94$, and we will show in §3.1.3 that a similarly narrow phase range for He emission occur in all of our RRab stars.

Inspection of the He I lines for the three earliest phases ($\phi = 0.856, 0.893, 0.912$) in the right-hand panels of Figure 1 reveals apparent He absorption in the 6678 Å line, but neither emission nor absorption in the 5876 Å line. The absorption seen at 6678 Å throughout most of the pulsation cycle is, in fact, due to Fe I not He I. Most lines of Fe I in the red spectral region of Fe I are very weak, but multiplet 268 (Moore 1972) is the exception with three strong lines: 6546.25, 6592.92, and

² <https://zenodo.org/record/5794389#.YcD3XBPMIo8>

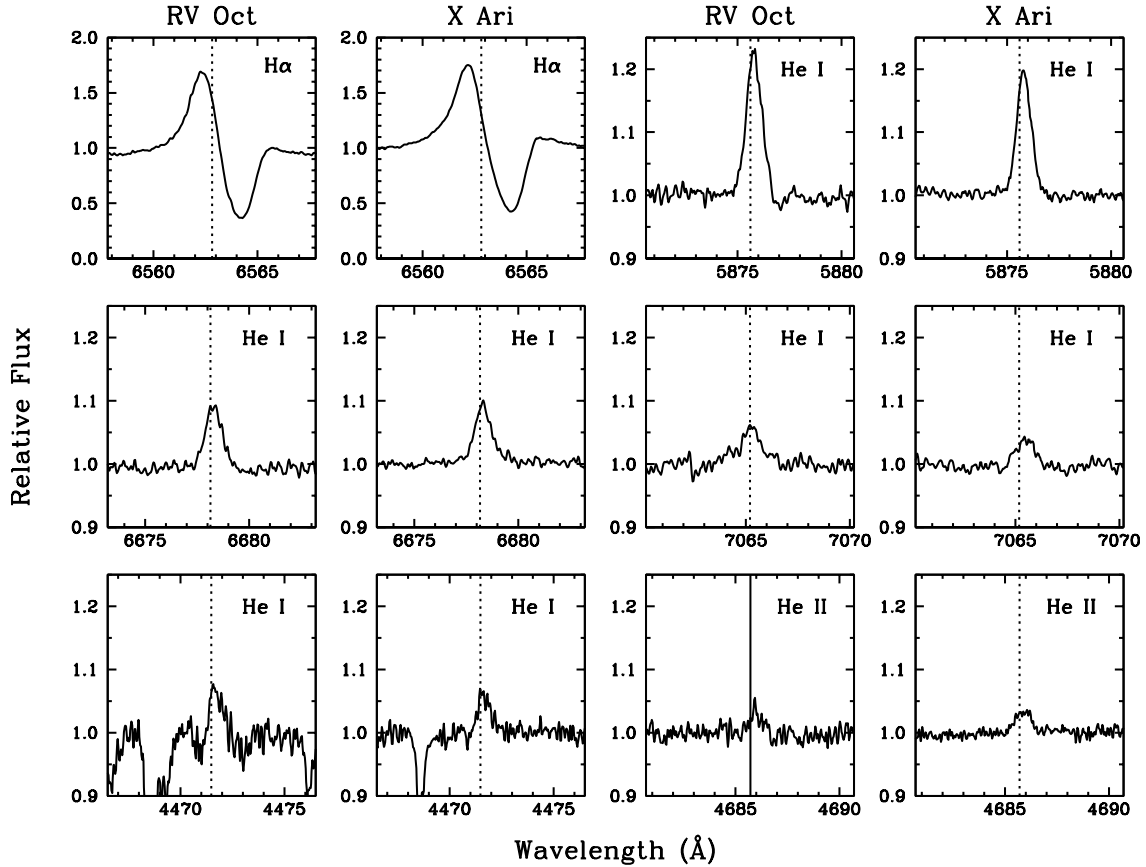


Figure 2. Mean line profiles of H α , four He I lines and a He II line at the phase of maximum He emission in program stars RV Oct and X Ari.

6677.99 Å. These lines have similar transition probabilities (Kramida et al. 2019)³ and have substantial absorptions in the solar spectrum (Moore et al. 1966). For $\lambda 6546$ $\log gf = -1.54$ and $EW_{\odot} = 103$ mÅ, somewhat blended with a weak Ti I line; for $\lambda 6592$ $\log gf = -1.47$ and $EW_{\odot} = 123$ mÅ; and for $\lambda 6678$ $\log gf = -1.42$ and $EW_{\odot} = 122$ mÅ. In the RV Oct phases shown in Figure 1 we always detected the $\lambda 6592$ line and tentatively identified $\lambda 6546$ above the continuum noise. However, the maximum-light phases under study here also have the highest photospheric temperatures. For RV Oct and other RRab stars, $\langle T_{\text{eff}} \rangle \sim 6150$ K at $\phi \sim 0.85$ but rises sharply in about an hour to $\langle T_{\text{eff}} \rangle \sim 7150$ K at $\phi \sim 0.95$ (For et al. 2011b). Neutral-species transitions such as those of Fe I weaken with rising temperature. If we examine the RV Oct spectrum at earlier phases, all three lines are easily detected. For our spectrum at $\phi = 0.370$ ($T_{\text{eff}} \sim 6100$ K, For et al. 2011b), the equivalent widths are $EW = 27$ mÅ for $\lambda 6546$, $EW = 35$ mÅ for $\lambda 6592$, and $EW = 44$ mÅ for $\lambda 6678$. All of these lines weaken to $EW \lesssim 5$ mÅ at $\phi \sim 0.9$, but our conclusion holds: the $\lambda 6678$ absorption is due to Fe I, not He I.

Preston (2009) showed spectra of the He I $\lambda 5876$ in emission during the rising-light phases of RV Oct, but also argued that four other He emission lines could be seen in these phases. In Figure 2 we show the presence of multiple He I lines in RV Oct and the very metal-poor X Ari, and one He

³ https://physics.nist.gov/PhysRefData/ASD/lines_form.html

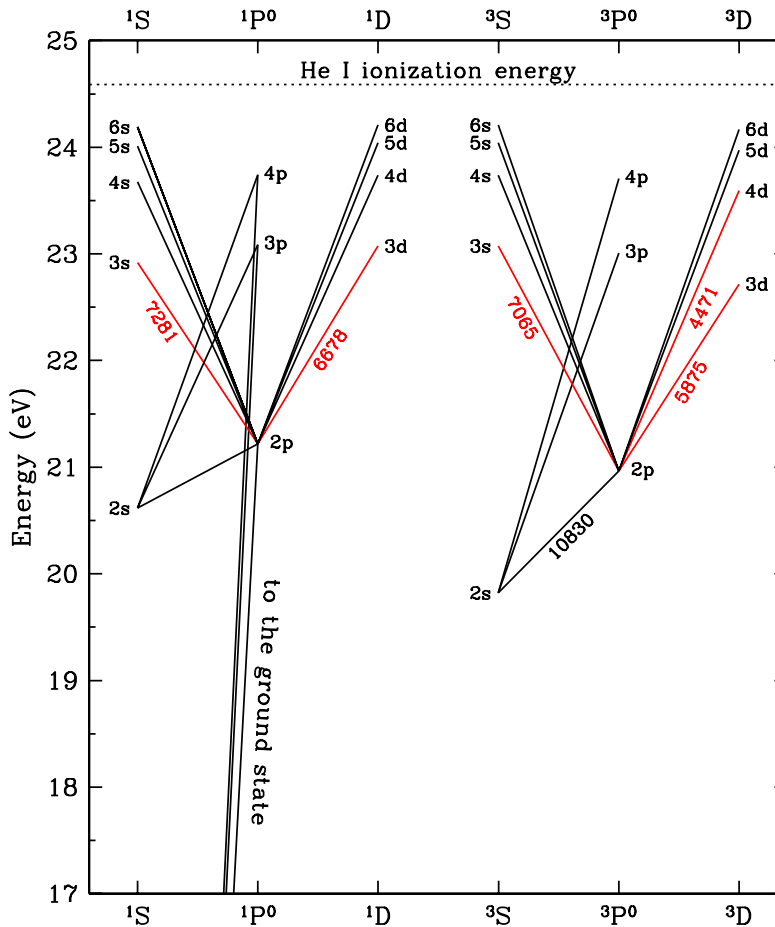


Figure 3. A partial Grotrian diagram for He I. Transitions detected by Preston (2009) are in red, with the wavelengths labeled. No permitted dipole transitions connect the triplet and the ground states.

II in both stars as well. To assist in these identifications, we co-added individual observations with maximum $\lambda 5876$ emission, five of them for RV Oct and eight for X Ari, thus substantially increasing their S/N values. The spectra that were combined were obtained essentially at a single phase for each star. Qualitatively the emission strengths are approximately the same in both stars.

The detected He I lines in RR Lyraes arise from very high excitation states of two multiplet systems. In Figure 3 we show a partial Grotrian diagram for this species, modeled after Moore & Merrill (1968), using data from the NIST atomic line database (Kramida et al. 2019)⁴. The very high excitation energies of the 2^1P and 2^3P He I transitions ensure that these lines detected in RR Lyrae stars cannot be formed in the same atmospheric layers that give rise to the metallic lines with typical excitation energies $\sim 1 - 3$ eV.

We omitted the 7281.48 \AA He I from Figure 2. This line is extremely weak in RV Oct and not obviously present in X Ari. Additionally, the $\lambda 7280$ spectral region is contaminated with many telluric H_2O features that were not cancelled in our reduction procedures, so we drop it from further consideration here. However, we should note that Zhang et al. (2005) found this transition most

⁴ <https://physics.nist.gov/PhysRefData/ASD/lines>

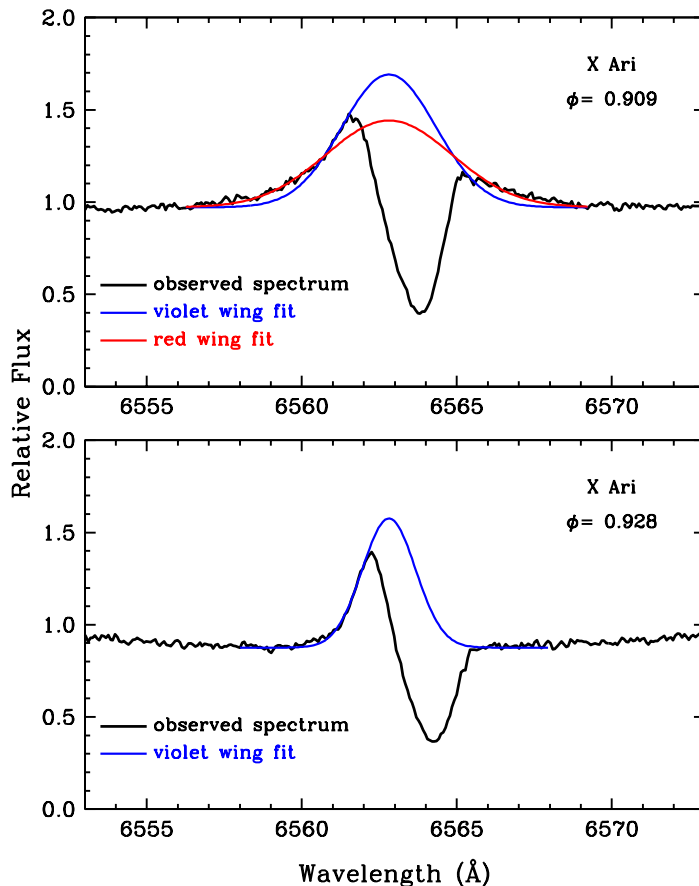


Figure 4. Two representative $H\alpha$ lines near emission maximum. Top panel: the $H\alpha$ profile in X Ari at phase $\phi = 0.909$ in one of its pulsational cycles (black line). A Gaussian profile is fitted to the violet wing of the observed emission (blue curve) ignoring the broad violet and red wings present in most stars near emission maximum. A second fit to the broad wings is plotted as a red curve. Bottom panel: the same Gaussian fit (blue curve) is made to the observed $H\alpha$ profile for the more typical case at a later phase, $\phi = 0.928$, when there is no red emission component to constrain the Gaussian velocity center. Because of the general absence of this constraint, we adopted the photospheric velocity defined by metal lines to locate the centroids of all Gaussian fits.

useful in constructing temperature diagnostics for planetary nebulae. We suggest that measures of He I $\lambda 7281$ in spectra with S/N higher than ours may prove useful in analysis of RRab shocks as well.

3. MEASUREMENTS OF EMISSION AND ABSORPTION LINES

3.1. The Emission Lines

The onset of observable shock waves in RRab stars always begins with the sudden, simultaneous appearance of H and He emission lines. These rise to maximum strength on time scales of minutes and decline on similar but slightly different timescales. They are followed by the appearance of violet- and red- displaced absorption components.

3.1.1. $H\alpha$ Emission Equivalent Widths

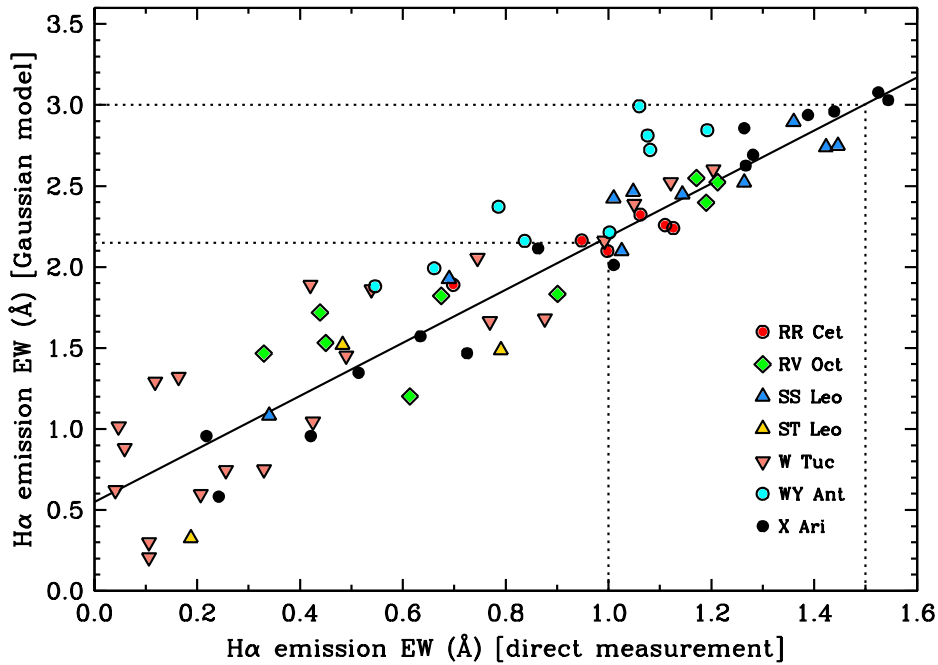


Figure 5. The correlation of $H\alpha$ emission equivalent widths measured by direct integration and a Gaussian model approximation, as defined in the text. Data between dotted lines show that Gaussian model EWs exceed measured values by a factor of 2.

We began with equivalent width (EW) measurements of the emission components of Balmer $H\alpha$ (6562.81 \AA). Measurements of EWs and wavelengths of the Balmer lines are complicated by the fact that the emission profiles are overlain (thus partially masked) by strong red-shifted absorptions of gas infalling from the previous pulsation cycle.

We measured the $H\alpha$ emission EWs in two ways: first by direct integration of emission parts of the observed features, and second by modeling the Gaussian pure emission profiles that best match the blue wings of the observed profiles. Our procedures are illustrated in Figure 4 for program star X Ari at two phases near maximum emission.

To effect direct integrations, we measured EWs of the violet emission fluxes in pixel ranges chosen by use of the IRAF (Tody 1986, 1993)⁵ *splot* e-cursor option. In Figure 4 for example, these ranges are $\sim 6557.0\text{--}6562.5 \text{ \AA}$ (top panel) and $6560.0\text{--}6562.5 \text{ \AA}$ (bottom panel).

For measurements of the Gaussian profiles we modeled the emission with Gaussians that best match the observed $H\alpha$ emission wings. Following Chadid & Preston (2013) we adopted the photospheric velocity defined by metal lines for the centers of our Gaussian fits. Then, as illustrated in Figure 4, we were presented with options for the best Gaussian approximations for the emission wings. Inspection of the observed $H\alpha$ in the top panel reveals that a single Gaussian cannot be fitted to the entire emission part of the total profile. In this case we fit a Gaussian to the violet component of X Ari at phase $\phi = 0.909$, ignoring the broad violet and red extensions, and a second fit to the broad extensions. The extended emission wings are a common, perhaps ubiquitous, characteristic of the $H\alpha$ emission profiles of RRab stars near emission maximum. They disappear at later phases, as

⁵ <http://ast.noao.edu/data/software>

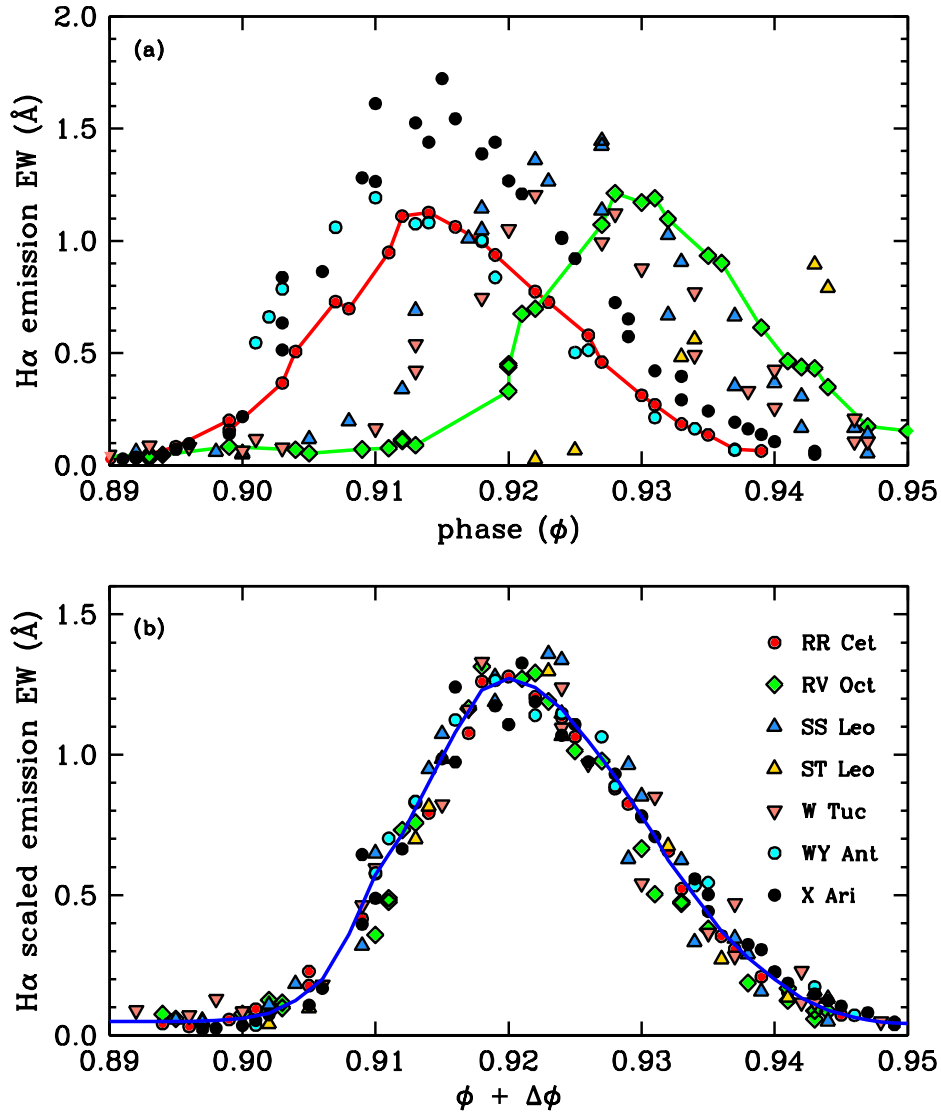


Figure 6. Top panel: H α emission EWs measured via direct integration plotted versus phases. For each star $\phi = 0.00$ was set to be the phase of minimum radial velocity. The red points for RR Cet and the green points for RV Oct have been connected with solid lines of their colors. Bottom panel: the emission EWs scaled to a common flux maximum and shifted to a common emission peak phase; see text for descriptions of these H α emission manipulations. Here the blue line represents the mean trend of scaled emission versus shifted phase. The symbols and colors of points are identified in this panel’s legend and are consistent with those of Figure 5.

illustrated in the Figure 4 bottom panel for X Ari at $\phi = 0.928$. The blue Gaussian emission wing had to suffice in the absence of a red emission component.

We compare our emission EWs from direct measurement with those derived from Gaussian model profiles in Figure 5. The two sets are clearly correlated, but there are systematic offsets between measures of different stars. Compare for example those of WY Ant (cyan-filled circles) and X Ari (black solid circles) in this figure. However, for the bulk of strong emissions (equivalent widths $EW > 1 \text{ \AA}$) the Gaussian model profile values exceed direct integration ones by a factor of ~ 2 , as shown by the solid line drawn through the data. The correlation is strongest for the strongest H α emission features, i.e., those contained between the dotted-lines in Figure 5 (data for WY Ant

excepted). Weaker emissions are more difficult to measure primarily because of uncertainty in proper continuum location. The systematic offsets and larger scatters in the regression for smaller EWs is evident in the figure.

The linear correlation between emission EWs derived from direct integration and from Gaussian model fits yields confidence that $H\alpha$ relative emission strengths can be derived from the observed line profiles. For the remainder of this paper we will employ the EWs from direct integration only, as these measurements involve fewer assumptions than those from Gaussian integration.

3.1.2. Phase variation of $H\alpha$ emission

The emission appears abruptly, rises to maximum on a timescale of a few minutes, and declines on a similar timescale, as illustrated in Figure 6 for seven RRab stars with the strongest emission in our sample. At first sight the data in the top panel seem to form a hopeless jumble. But inspection quickly reveals that the jumble is caused largely by systematic star-to-star phase shifts. This is illustrated by lines connecting the data for RR Cet (red) and RV Oct (green). The points for these two stars can be superposed in phase by applying mean shifts of $+0.0060$ and -0.0095 to the RR Cet and RV Oct, respectively.

By trial and error we found phase shifts, $\Delta\phi$, that align all emission maxima at an arbitrarily adopted phase $\phi = 0.92$. These phase shifts are listed in Table 2. Additionally, we used the absolute fluxes of Kurucz (2011, 2018)⁶ model atmospheres to convert measured fluxes in the du Pont echelle orders to fluxes relative to the continuum flux at $H\alpha$, all scaled to the average value of these measurements in the phase interval $0.915 < \phi + \Delta\phi < 0.925$. We applied these flux normalizations and small phase shifts to the emission phase data for the seven stars in the top panel of Figure 6 to produce the much more coherent flux versus phase variation in the bottom panel. A blue-colored line in this panel represents the mean trend of these data. The small scatter of individual points from this line, $\sim \pm 0.002$ in shifted phase, $\sim \pm 0.1$ in scaled EW, strongly suggests that this is a standard feature in $H\alpha$ behavior near maximum light in metal-poor RR Lyraes.

3.1.3. Helium I Emission

Identifications of five emission lines of He I were reported by Preston (2009) in du Pont echelle spectra of RV Oct during rising light. We restrict attention to the leading lines of the series ($^3P^0 - ^3D$), 5876 \AA , and ($^1P^0 - ^1D$), 6678 \AA , because they are the only lines measurable in substantial numbers of the spectra obtained in our survey. The behaviors of these two lines are much simpler than those of Balmer lines. Because of their much larger excitation energies ($>20 \text{ eV}$), the He I series do not produce detectable absorption by infalling gas during the initial emission line phases. This simplicity is clearly illustrated in the middle panels of Figure 1 (phases $\phi = 0.927, 0.928$) above. Therefore, flux and velocity measurements can be made without regard to the complications encountered above for $H\alpha$.

Emission EW measurements of 5876 \AA and 6678 \AA were made in the same manner as described in §3.1.2 for $H\alpha$. Peak EWs for these He I lines are smaller than that of $H\alpha$ by factors of 6 and 12, respectively, so measurements were limited to a smaller range of phases, and measurement accuracies were reduced accordingly.

⁶ Available at <http://kurucz.harvard.edu/grids.html>

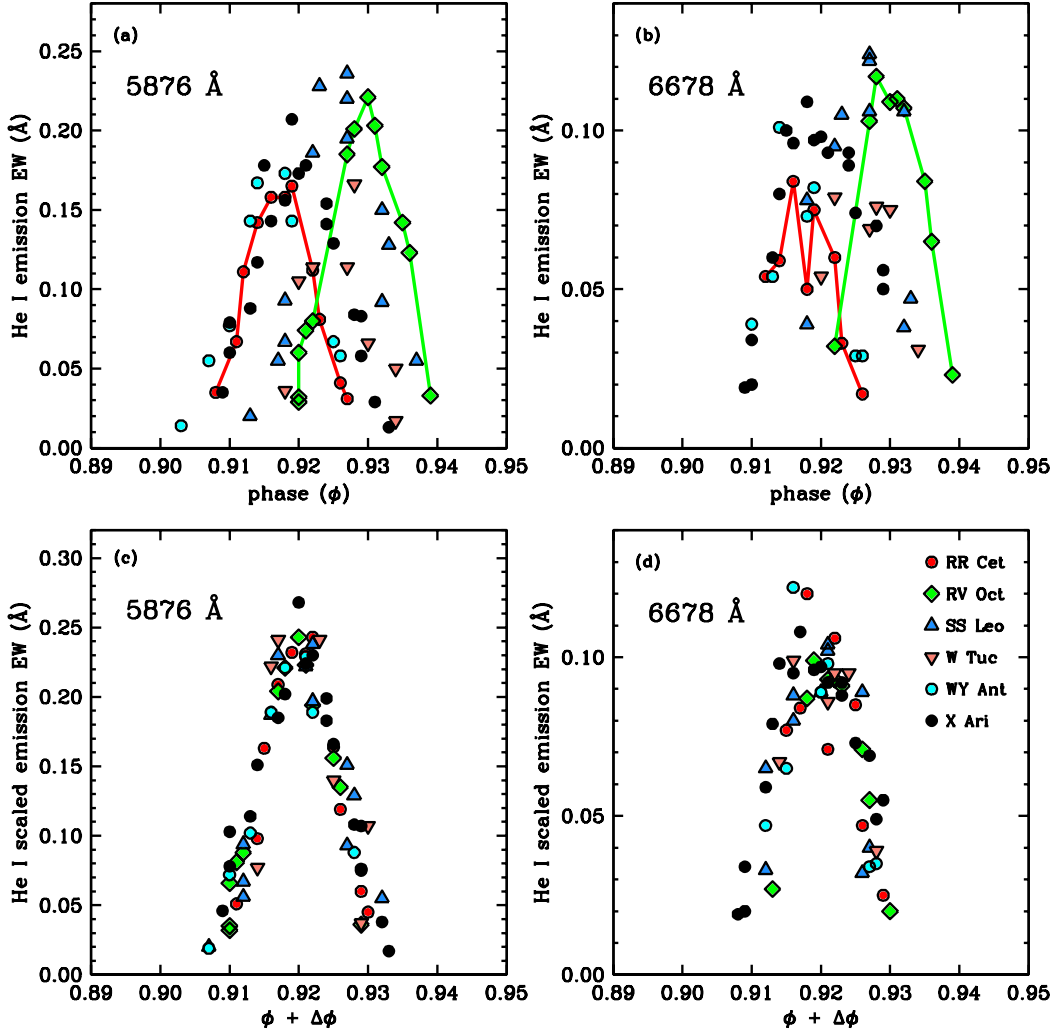


Figure 7. Measured EWs (top panels) and scaled emission EWs shifted to phase = 0.92 (bottom panels) for He I 5876 Å and 6678 Å in the manner employed for H α in Figure 6. The symbols and colors of points are identified in panel (d) and are consistent with those of Figure 5

In Table 2 we list the estimated phase shifts $\Delta\phi$ for He I 5876 Å needed to construct Figure 7 (b). We emphasize that the phase shifts $\Delta\phi$ for He I 5876 Å emissions were determined independently from those derived for H α described in §3.1.2. Although both lines arise in the recombination wake of the shock, the two line forming regions cannot be identical because of the large difference in the ionization potentials (~ 11 eV) of H I and He I. Figure 8 shows that the two shifts are strongly correlated, but the slope of the regression is less than unity.

3.1.4. Helium II $\lambda 4686$ Emission

As noted in §2.2, He II 4686 Å $3^2D-4^2F^o$ is analogous to H I Paschen α . Preston (2009) reported weak He II 4686 Å emission in three Blazhko variables (AS Vir, UV Oct, and V1645 Sgr) observed during large amplitude cycles when their metallic-line radial velocity amplitudes were 65, 70, and

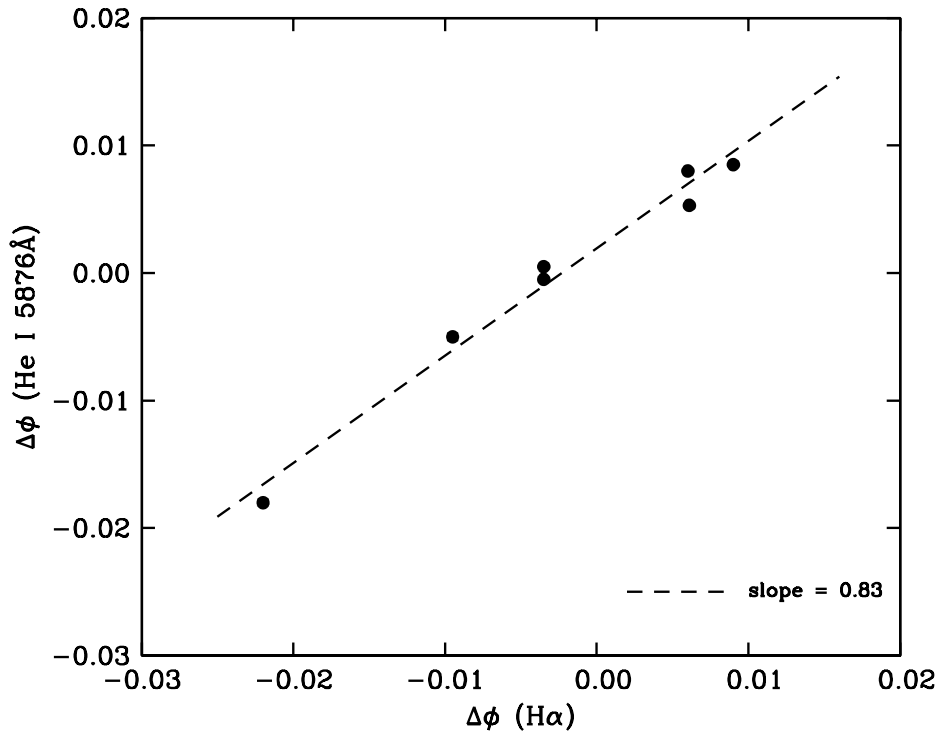


Figure 8. Phases that produce alignment of emission maxima for He I 5876 Å are plotted versus those for H α . The two shifts are strongly correlated

64 km s⁻¹, respectively.⁷ These emission lines together with those of five stable RRab with similar RV amplitudes are displayed in Figure 9. The average spectrum formed from these spectra at the top of the figure shows unambiguous detection of the He II line. The largest measured equivalent widths in Figure 9, i.e., those for RV Oct and X Ari, are ~ 30 mÅ.

By converting average Blazhko RV amplitude for AS Vir, UV Oct, and V1645 Sgr, 66.3 km s⁻¹, to pulsation amplitude, dR/dt ⁸ with projection factor, $p = 1.3$, we obtain an estimate of a critical pulsation velocity amplitude, 82 km s⁻¹, above which observable $\lambda 4686$ He II emission occurs in our spectra.

We chose projection factor $p = 1.3$ for calculation of dR/dt after review of the p -values, derived by a variety of methods, that are summarized in Figure 5 of Neilson et al. 2012). These p -values, all sensitive to assumptions about limb darkening and atmospheric stratification, range from 1.2 to 1.4. We adopt a conservative one decimal-place value for p that reflects our uncertainties about RRab atmospheric parameters, particularly during rising light.

Finally, strong absorption due to Mg I at $\lambda 4703$ illustrates the seemingly paradoxical occurrence of lines of He II (IP = 54.4 eV) and Mg I (IP = 7.6 eV) in the same spectra. This circumstance requires pronounced temperature stratification in the shock wake, to be discussed in a work in progress.

3.2. Absorption Lines

⁷ Details of the radial velocity measurement procedure may be found in Preston & Sneden (2000) and Chadid et al. (2017).

⁸ We derive the pulsational velocity dR/dt in the stellar rest frame using formula (1) in Chadid et al. (2017), as described in their §4.3.

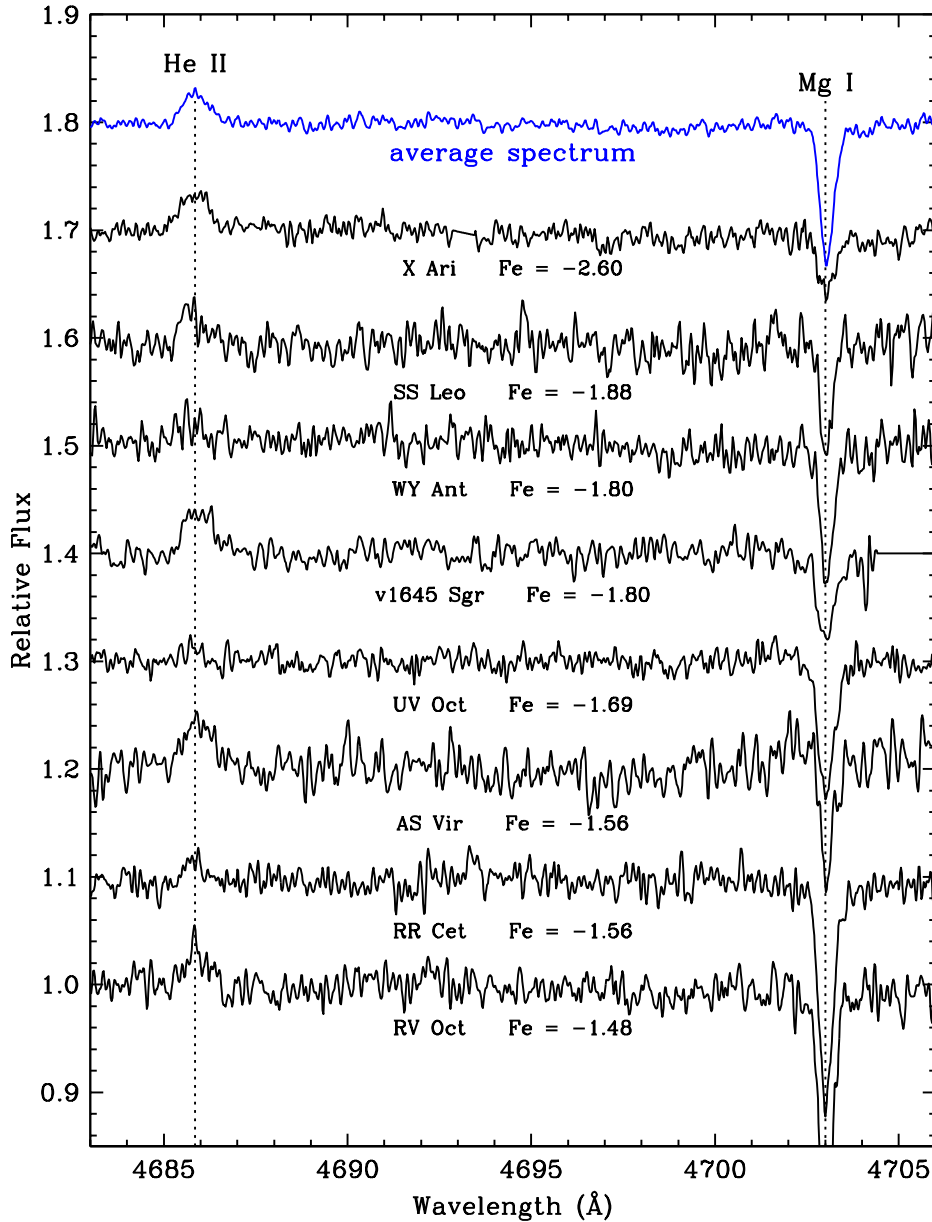


Figure 9. Spectra of the He II 4686 Å region of eight RRab stars arranged bottom to top in order of increasing $[\text{Fe}/\text{H}]$. The relative flux values for RV Oct are correct, and the spectra for the other stars are shifted vertically for display purposes. The average spectrum shown in blue at the top of the plot was formed by a straight mean of the individual spectra. Dotted vertical lines are located at the rest wavelengths of the He II line and the photospheric Mg I line.

Immediately after the phase of maximum emission, red-shifted absorption lines of H and He begin to appear in most metal-poor RRab spectra. This section is devoted to a description of their behavior.

3.2.1. $H\alpha$ Absorption

We measured three quantities useful for discussion of atmospheric structure during rising light: radial velocities (RV km s^{-1}), equivalent widths (EW Å), and Doppler widths ($\sigma_{\text{Max}} \text{ km s}^{-1}$). To accomplish this task we used IRAF/plot with the “d” cursor option. σ_{Max} is the Maxwellian line-

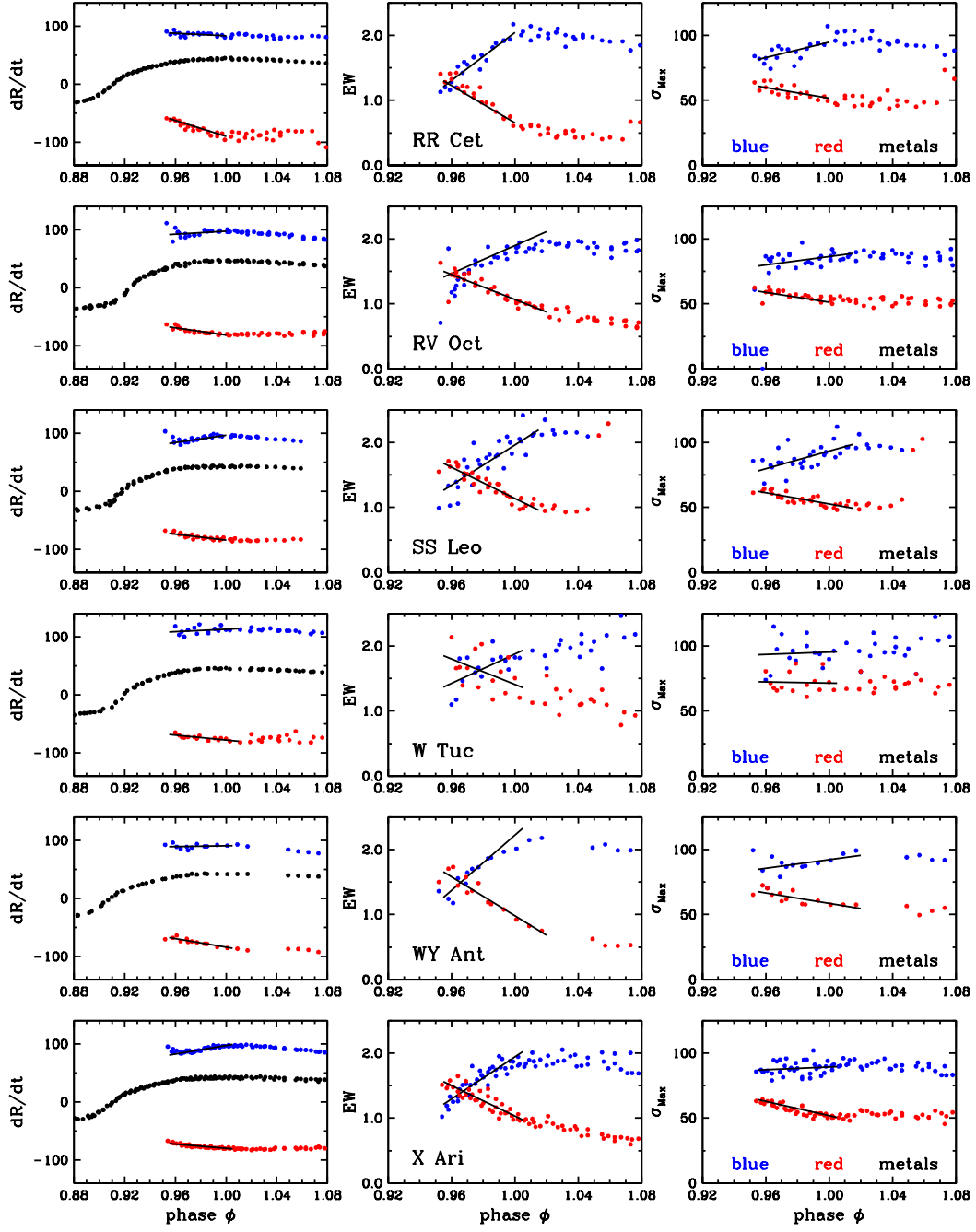


Figure 10. The variations of H α pulsation velocity dR/dt (km s^{-1}), equivalent width EW ($\text{m}\text{\AA}$), and Maxwell line-of-sight velocity dispersion σ_{Max} (km s^{-1}) with phase during rising light for six RRab stars. Red and blue symbols are measures of lines produced by infalling and out-flowing atmospheric layers, respectively.

of-sight velocity dispersion defined by equation 1 of Unsöld & Struve (1949) We display the phase variations of these quantities for six RRab stars in the montage of Figure 10. Values of the pulsation velocities dR/dt and velocity dispersions σ_{Max} of the H α absorptions at phase ~ 0.97 , when they first become measurable, are given in the top half of Table 3.

The average H α velocity difference between infall and outflow in column 4 of Table 3 is about twice the range of the continuous velocity variation of the metal lines. Radial velocity is a location

marker in the atmosphere. Metal lines are formed in the region where continuum optical depth is $\tau \sim 0.1\text{--}0.2$, near the photosphere ($\tau \sim \frac{2}{3}$), while the heavily saturated cores of H α produced in the outflowing and infalling gas must be formed high in the atmosphere at very low continuum optical depths. The large persistent differences between H α and metal velocities when both are measured during rising light signal the existence of velocity gradients in the atmosphere detected by Chadid & Gillet (1996) and discussed by Bono et al. (1994) and Fokin & Gillet (1997). These gradients produce line asymmetries that will be the subject of a paper in preparation.

The regression coefficients used to construct the phase variations in Figure 10 for dR/dt and σ_{Max} are given in Table 4. We chose linear equations for all regressions with one exception: the large S/N values of the σ_{Max} data for X Ari permitted use of a quadratic fit. We see a tendency for maxima in σ_{Max} near phase 0.97 in the outflows of the other five stars, so we surmise that this quadratic behavior may well be a general characteristic of the MP stars that is best studied with higher S/N than that available in our spectra.

Two H α absorption components appear near phase 0.96 and remain measurable after maximum light for durations that vary greatly from star to star. The average difference between infall and outflow velocities, characteristically $\sim 165 \text{ km s}^{-1}$ near maximum light, differs little from star to star in our sample. This similarity is due at least in part to a selection effect created by our choice of RRab stars with strong H α emission.

The EWs of the outflow (B) and infall (R) components are approximately equal ($\sim 1.5 \text{ \AA}$) at phase 0.97 for all six stars discussed here. The outflow values continue to increase for some 0.02 cycles past RV minimum. Thereafter, they remain constant or decline slightly. The infall EWs decline continually after their first appearance, more slowly after phase 0.02, and they generally persist beyond phase 0.10. Remarkably, infall absorption for RV Oct can be measured to phase 0.2.

The line-of-sight velocity dispersions for H α are residual values after removal of instrumental broadening by Gaussian deconvolution, and much smaller effects due to thermal broadening, microturbulence and the Stark effect. We discuss the (lack of) a significant contribution by the Stark effect to our measured line widths in §3.2.3.

Outflow dispersions at phase 0.97 are typically $\sim 90 \text{ km s}^{-1}$, then they generally increase slightly until phase of RV minimum, and remain constant thereafter until the lines disappear. Infall dispersions at phase 0.97 are smaller ($\sim 62.0 \pm 5.7 \text{ km s}^{-1}$), decline slowly and remain approximately constant at $\sim 50 \text{ km s}^{-1}$ until they disappear. W Tuc is an apparent exception. Our measures of its infall dispersion yield a constant value of $72.0 \pm 6.9 \text{ km s}^{-1}$ in the phase interval $0.97 < \phi < 1.10$.

3.2.2. He I Absorption

We computed the same absorption quantities dR/dt (km s^{-1}), EW (m\AA), and σ_{Max} that were derived for H α . These are displayed in Figure 11. Because He I 5876 \AA is much weaker than H α we co-added files into phase bins of 0.01P for this figure. Emission features are included in the regression for dR/dt to illustrate the continuity with outflowing absorption that is expected, because the emission and blue absorption features must arise in the wake of the shock.

The small values of dR/dt for He $\lambda 5876$, similar to those for the metal lines in the early expansion phases ($0.90 < \phi < 0.95$), surprise us because the thermal conditions for the production of metal lines and He $\lambda 5876$ are so different. Likewise, the velocity dispersion at these phases are also similar to those of the metals at these phases reported in considerable detail by Preston et al. (2019). Note

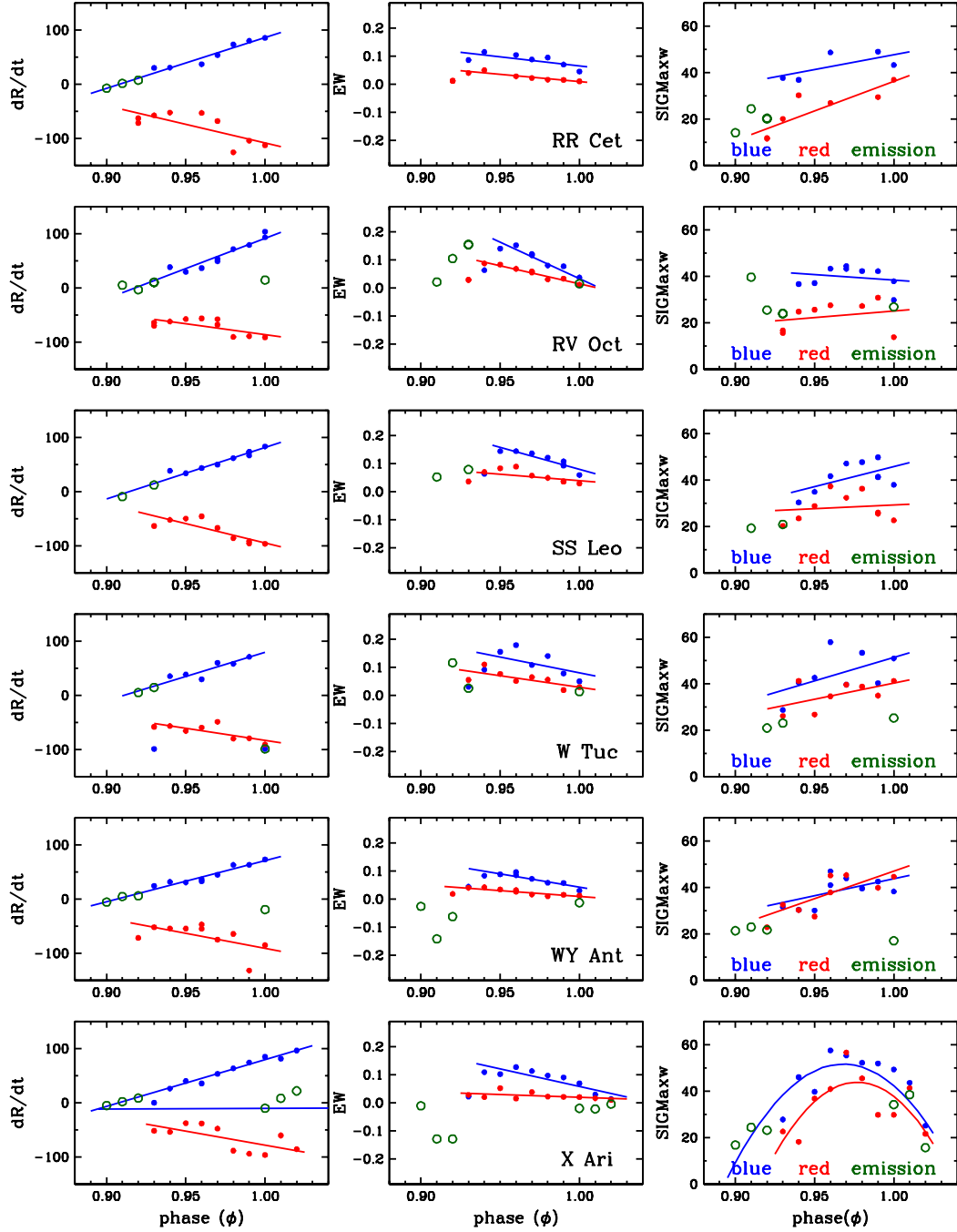


Figure 11. (left) The variations of He I pulsation velocity dR/dt (km s^{-1}), (middle) equivalent width EW ($\text{m}\text{\AA}$), and (right) velocity dispersion σ_{Max} (km s^{-1}) with phase during rising light for the same six RRab stars shown in Figure 10. Red and blue symbols are measures of lines produced by infalling and outflowing atmospheric layers, respectively. Unfilled dark green symbols denote emission features.

also the reappearance of He $\lambda 5876$ emission in the post maximum spectra of RV Oct, WY Ant, and X Ari, first reported for RV Oct in Preston (2009). This reappearance is discussed in §4 below.

We interpret the He $\lambda 5876$ data in a preliminary way by superposing it on the $H\alpha$ data for six stars in Figure 12. Integration of the He $\lambda 5876$ regression from the inception of emission until it reaches the outflow velocity of $H\alpha$ produces an estimate of the distance traversed by the shock from the phase

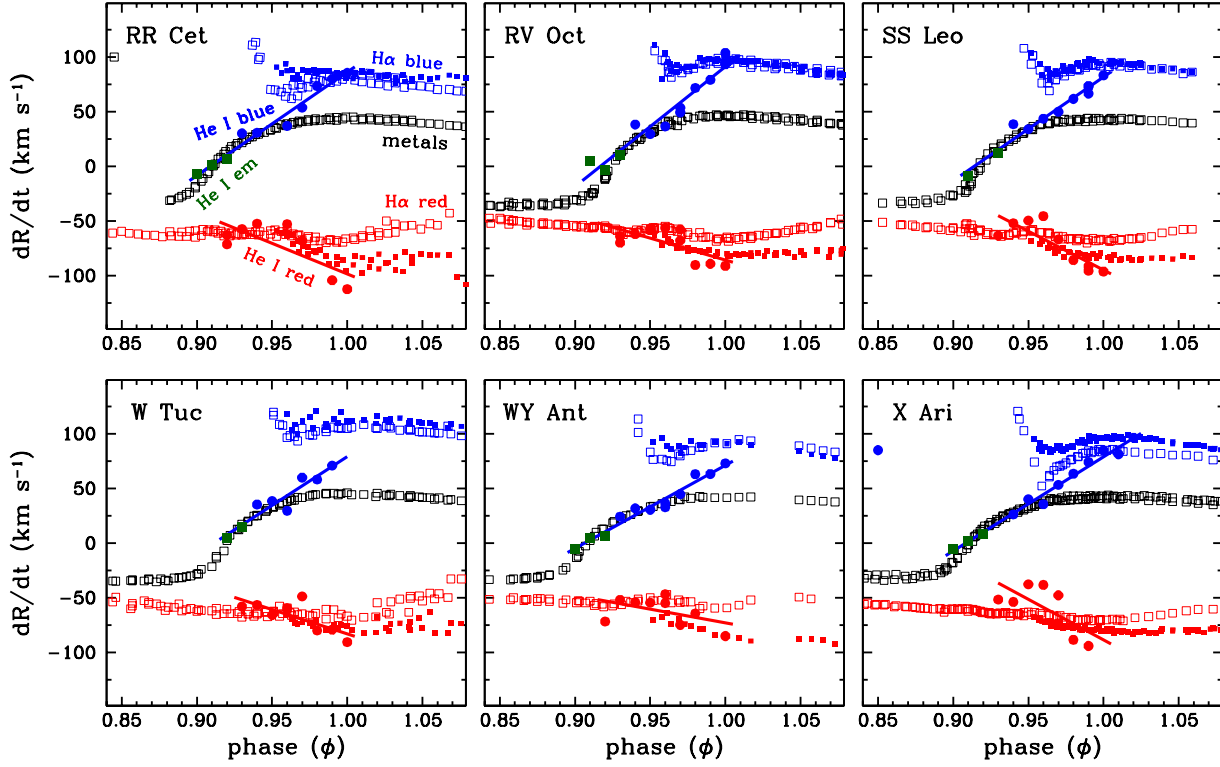


Figure 12. H α and He I pulsation velocities from the left-hand windows of Figures 10 and 11 combined in one panel each for the six stars. The symbol colors are labeled in the panel for RR Cet. Squares are used for the *Halp* data; open squares denote those measurements made with IRAF *fxcor*, and filled squares for those made with IRAF *splot*. Data points for He 5876 Å in this Figure represent more data than do those in Figures 10 and 11 because of co-addition.

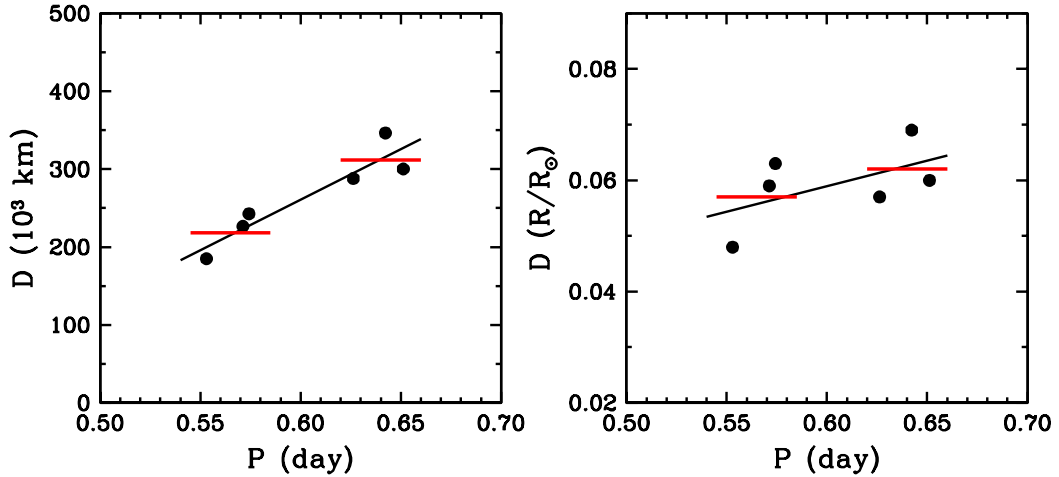


Figure 13. The distance D traversed by the primary shock from the metallic line-forming region just above photosphere to the layer that produces out-flowing H α absorption. In the left panel D is expressed in units of km, and in the right panel D is shown in units of stellar radii. Data for six stars are taken from Table 13. Black lines show the mean trend of the data from a linear regression. Red lines show radii for Oo I and II groups taken from Table 1 of Marconi et al. (2005).

of emergence from the photosphere to its arrival at the level of formation of the $H\alpha$ absorption. The results of such integration for our six stars are shown in Figure 13.

Although not important in the context of our investigation, we call attention to the systematic differences between $H\alpha$ velocities measured with IRAF/*splot-d* and IRAF/*fxcor* evident in Figure 12. These differences are largest in the weak infalling (R) post-maximum components. *splot-d* employs a deblending procedure that attempts to recover the (Gaussian) central wavelengths, EWs, and FWHMs of the B and R components by a best fit algorithm. The *fxcor* measurements rely on the measurer’s choice of pixels to include in the *fxcor* sampling of the blended B and R components. This choice is difficult to make for the R component when it appears as a weak feature in the red wing of a strong B component. Accordingly, we use the *splot-d* results in our discussion, including the *fxcor* data in Figure 12 only as a warning to those who might contemplate similar measurements.

3.2.3. Stark Broadening

After correcting measured FWHMs for instrumental, thermal and microturbulent broadening by use of Gaussian subtraction we converted FWHM to Maxwellian line-of-sight velocity dispersion as described in Preston et al. (2019) and presented in Table 3 and in the right-most panels of Figures 10 and 11. Before discussing these results we consider whether or not Stark broadening, a common effect in stellar lines of H and He, contributes to the widths of the Doppler cores of $H\alpha$ and He I $\lambda 5876$ in RRab atmospheres, here taken to have characteristic values of $T_{\text{eff}} = 7,000$ K and $N_e = 10^{14}$ cm $^{-3}$.

For $H\alpha$ Kowalski et al. (2017) calculate FWHM = 0.14 Å ($\sigma_{Max} = 5$ km s $^{-1}$) for the parameters ($T_{\text{eff}} = 10,000$ K and $N_e = 10^{14}$ cm $^{-3}$) that they deem appropriate for solar and stellar flares. This value agrees well with a three order-of-magnitude downward extrapolation of the regression of Griem (1983) for $T = 20,000$ K used by Kielkopf & Allard (2014) as a fit to laboratory data collected in the range $10^{17} < N_e < 10^{21}$. We conclude that Stark broadening is an insignificant contributor to our σ_{Max} values for $H\alpha$ in MP RRab stars.

For He I $\lambda 5876$ Å we refer to the regression used by Gigoso et al. (2014) in their Figure 24b to fit data obtained in a number of laboratory experiments. A small justifiable extrapolation of their regression to stellar N_e values indicates that the Stark effect produces a negligible broadening of this line at $T < 10,000$ K, $N_e = 10^{14}$ cm $^{-3}$.

Accordingly, in the absence of any additional broadening processes, we conclude that the σ_{Max} values in Table 3 and Figures 10 and 11 are reliable measures of line-of-sight velocity dispersions that occur in MP RRab atmospheres during primary light rise.

4. THE NATURE, ORIGIN AND PERSISTENCE OF HE LINES IN RRAB

Our discussion centers on Figures 14 and 15. In these figures dashed vertical lines are plotted at the rest wavelengths of metal lines, which are formed in the near-photosphere gas layers. We derived these rest wavelengths by cross-correlation of metallic-line spectra in the wavelength region 4000–4600 Å, using IRAF/*fxcor* as discussed by Preston & Sneden (2000). Masks removed Balmer $H\delta$ and $H\gamma$, and the great majority of metallic absorption lines that create the cross-correlation signal are those of Fe I with excitation potentials between 1 eV and 3 eV. Dashed verticals at rest wavelengths closely bisect the He I 5876 Å emission features in all stars of both figures, but they lie slightly red-ward of the $H\alpha$ emission maxima as expected from the considerations in §3.2.1. The weak He I lines in metal-rich

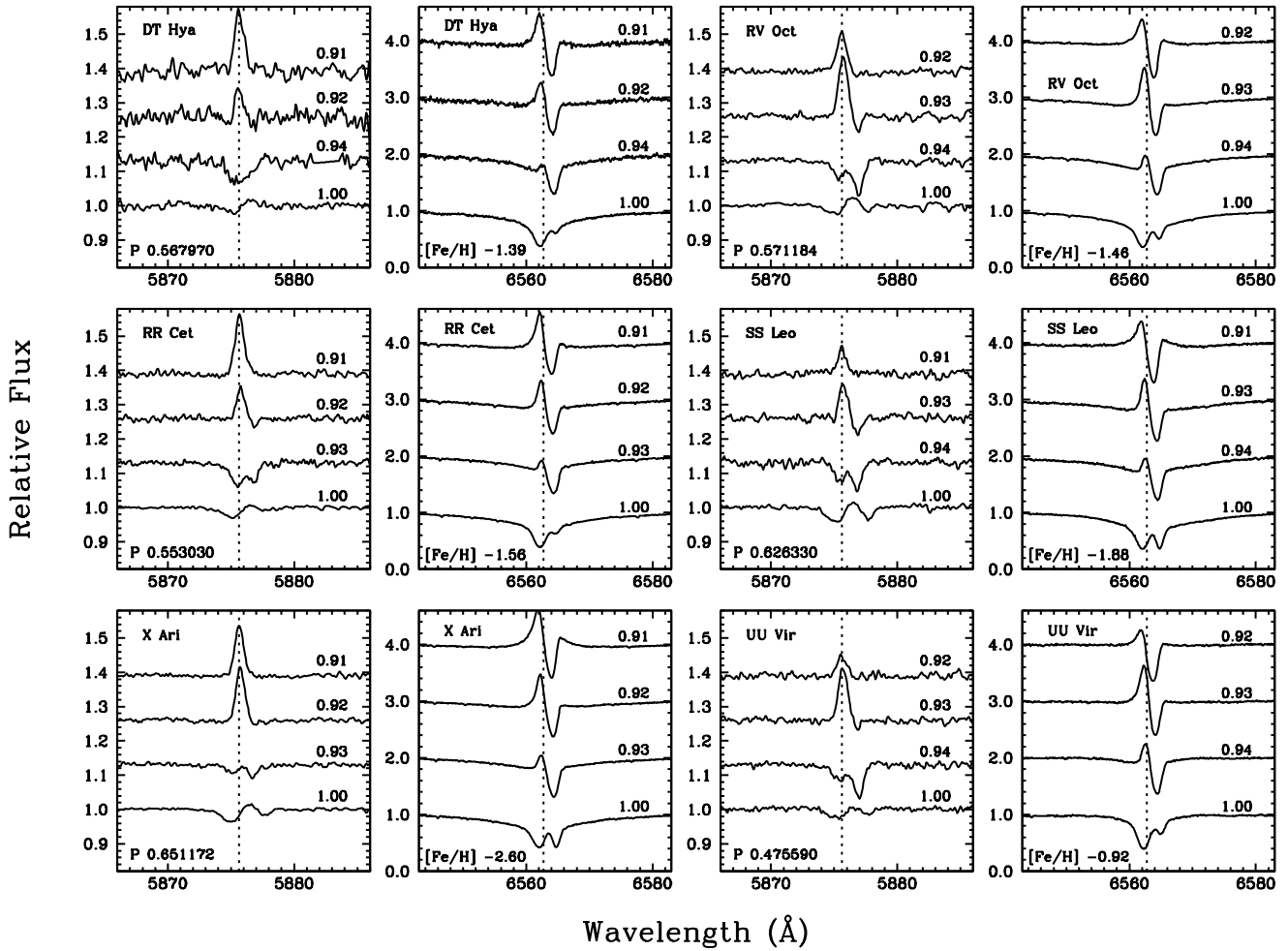


Figure 14. Line profiles of He I 5876 Å and H α for six metal-poor RRab at four pulsation phases.

stars conform to expectations based on H α in Chadid et al. (2017). However, time-evolution of the line profiles of He I 5876 Å and H α in these figures pose several problems.

In previous investigations we divided our stars into metal-poor and metal-rich abundance groups at $[\text{Fe}/\text{H}] = -1$, rounding to the nearest integer the abundance boundary, -0.8 , used by Zinn (1985) to separate disk globular clusters from those of the halo. Here we revert to Zinn’s division point, primarily because it places UU Vir among the metal-poor RRab, where it belongs in Figures 14 and 15 and in the various correlations presented in Chadid et al. (2017). That such precision in choice of the division point affects our discussion strongly suggests, that the boundary is, in fact, blurred, i.e., the abundance distributions of halo and disk overlap. We reject the notion that UU Virginis is a class *sui generis*.

Following expectations of Schwarzschild’s (1952) model, we locate the H and He emissions in outward-flowing gas following its passage through a strong shock (Wallerstein 1959). The different appearances of the initial emission line profiles of He and H arise as a circumstance imposed by infalling gas. H is so abundant that it produces absorption in atmospheres of all stars, types O through M. Infalling gas above the shocks will have temperatures that are consistent with those implied by broad-band colors and metallic lines in the spectra ($T \sim 6500$, e.g., For et al. 2011b). This gas is responsible for the strong red-ward displaced H α absorption. Because He I lines, all

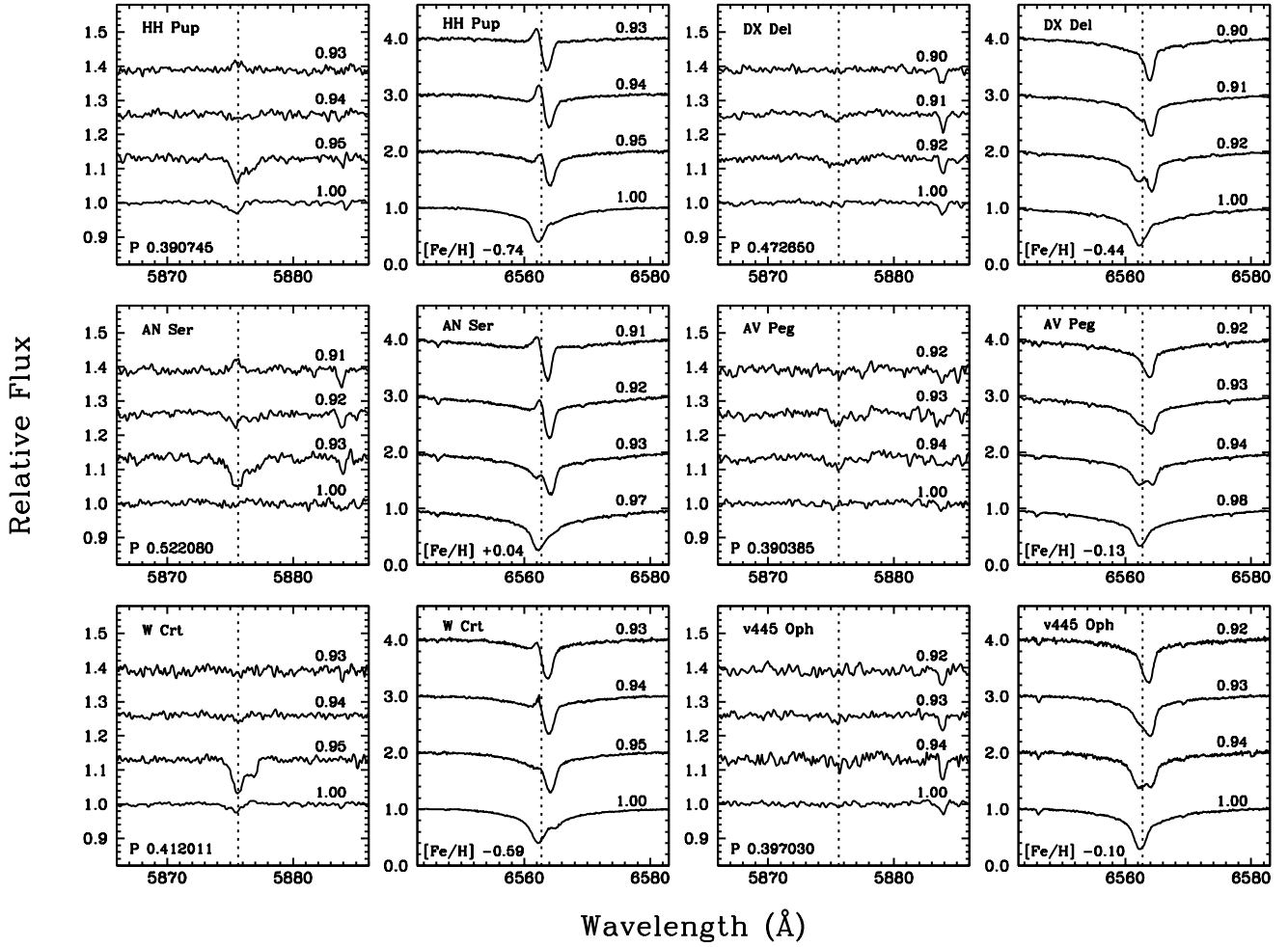


Figure 15. Line profiles of He I 5876 Å and Hα for six metal-rich RRab at four pulsation phases.

with excitation potentials > 20 eV (Figure 3), occur only in OB atmospheres with $T_{\text{eff}} > 10,000\text{K}$, He emission flux produced in the wake of the shock is not distorted initially by absorption of infalling gas. Therefore $\lambda 5876$ is an ideal diagnostic for investigating the time-evolution of shocks in RRab atmospheres.

However, issues arise with the evolution of He 5876 line profiles presented in the top three spectra for each star in Figure 14. Stars in this Figure are arranged in order of decreasing maximum emission flux (from DT Hya upper left to UU Vir lower right). He absorption in the infalling gas appears in all six stars at or soon after phase 0.92. It strengthens initially as emission declines and it persists long after the observable emission disappears. This behavior is particularly noticeable in the panels for X Ari, RV Oct, SS Leo, and UU Vir.

The origin of infalling He I 5876 Å absorption presents a puzzle. The p^3P^o level of He $\lambda 5876$ is metastable: radiative excitation from the 1S ground state to this state is forbidden, and in any event the lifetime of 2^3P^o is a mere 5.63 ms (Lach & Pachucki 2001; Hodgman et al. 2009). In contrast, prominent $\lambda 5876$ absorption ($\text{EW} \sim 50 \text{ mÅ}$) is present in infalling gas throughout the phase interval $0.92 < \phi < 1.00$, persisting for ~ 1 hour after the phase of emission maximum as illustrated in Figures 11 and 14.

Collisional excitation cannot populate the 2^3P^o level of infalling He because this gas has not yet reached the shock. So, how is this level populated? The only remaining possibility is recombination following ionization by a source of “hot” radiation. However, the broad-band colors of these stars during rising light of by [Monson et al. \(2017\)](#) provide no convincing evidence for such a long-lived source of hot radiation that would have to be present during all of the rising branch of the pulsation cycle and beyond.

Next, we call attention to an unexpected change in the He I 5876 Å profiles that occurs during a few minutes near phase 0.97, intermediate between the phases of the bottom two spectra in each panel of Figure 14. Such variations of this line profile, first noted in spectra of RV Oct ([Preston 2009](#)), are reminiscent of the profile variations of Fe II $\lambda 4923$ encountered in the Blazhko variable S Arae by [Chadid et al. \(2008\)](#), and attributed by them to a hypersonic shock that develops high in the atmosphere. Our He I phenomenon is seen most clearly by comparing the bottom two spectra of panels for X Ari, RV Oct, SS Leo, and UU Vir of Figure 14. The symptoms of this phenomenon, present in varying degrees in all RRab stars in our survey, are these:

1. The profile suddenly broadens dramatically. The average radial velocity of the red-shifted absorption for the stars in Figure 14 (DT Hya excepted) increases from $60.3 \pm 3.7 \text{ km s}^{-1}$ to $105.0 \pm 1.9 \text{ km s}^{-1}$ while that for the violet-shifted component decreases from $-10.5 \pm 8.0 \text{ km s}^{-1}$ to $-23.4 \pm 6.5 \text{ km s}^{-1}$. The extent to which the measured absorption velocities are shifted from their true positions by putative emission wings is unknown.
2. The velocity of the violet-shifted component is difficult to quantify unambiguously because of its asymmetry; the violet wing RV Oct extends approximately to an escape velocity, $\sim 200 \text{ km s}^{-1}$, calculated for canonical values of the mass ($0.65 M_{\odot}$) and radius ($5.5 R_{\odot}$).
3. Weak ($\sim 2\%$) emission reappears between the absorption components. Chi-square analysis confirms its reality in X Ari, RV Oct, and SS Leo. It is a reality to be reckoned with.

Finally, we consider the incongruent properties of two stars lying together at top-left in Figure 15.

1. HH Pup, contrary to expectations due to its weak H and He emissions, has the largest photometric (1.35 mag) and radial velocity (69.7 km s^{-1}) amplitudes and the largest primary acceleration in our entire spectroscopic sample ([Chadid et al. 2017](#)). It also has the shortest pulsation period (0.39 d), which it shares with AV Peg (also in the mid-right panels of Figure 15). It is an archetypal example of the low latitude, short period RRab population first identified by [Kukarkin \(1949\)](#) and subsequently as metal-rich by [Preston \(1959\)](#), [Layden \(1994\)](#), and [Layden et al. \(1996\)](#).
2. AN Ser, the most metal-rich star in our sample, $[\text{Fe}/\text{H}] = +0.04$, has by far the longest photometric period (0.52 d) of the metal-rich RRab. It belongs neither to Oosterhoff’s type I metal-poor cluster population, nor to Kukarkin’s short-period low-latitude metal-rich population. Note that DX Del ($P = 0.47 \text{ d}$, $[\text{Fe}/\text{H}] = -0.44$) in the right column of Figure 15 is a cousin of HH Pup.

Location of HH Pup, AN Ser, and DX Del in a proper evolutionary sequence of stellar populations is a challenge for the future. We continue to seek explanations of results presented above. We defer

our exploration of the systematically weaker H and He emission in metal-rich RRab to a paper in preparation.

5. SUMMARY

We report quantitative data about spectral features of $H\alpha$, He I, and He II measurable with spectra obtained during the course of an 8-year survey of some three dozen RRab stars with representative periods and metallic abundances. We present graphical and tabular descriptions of the time evolutions of the emission line equivalent widths of $H\alpha$, triplet He I $\lambda 5876$, and singlet He I $\lambda 6678$ of RRab stars with strongest He I emission. We also show time evolutions of the radial velocities, equivalent widths, and turbulent velocities of $H\alpha$ and He I $\lambda 5876$ absorptions measured for outflow and infall gas during the shock phases.

A principal conclusion of our work is that radial velocities of He I $\lambda 5876$ define outward traveling waves in metal-poor RRab that we use to estimate the extent of RRab atmospheres traversed by the primary shock waves. We call attention to the problem of populating the 2^3P^o level of He I in infalling gas during primary shock phases. We identify several RRab that do not fit in extant theory of Galactic stellar evolution. Finally we provide well-documented evidence for the occurrence of He II $\lambda 4686$ emission in eight RRab stars during primary light rise.

As always we thank the support staff for their efficient, cheerful assistance in our work at LCO. We also thank Giuseppe Bono and Harriet Dinerstein for helpful comments that improved our presentation. This work has been supported by NSF grant AST-1616040 (C.S.).

Facilities: Du Pont (echelle spectrograph)

Software: IRAF (Tody 1986, Tody 1993), SPECTRE (Fitzpatrick & Sneden 1987)

REFERENCES

- Bono, G., Caputo, F., & Stellingwerf, R. F. 1994, *ApJL*, 432, L51, doi: [10.1086/187509](https://doi.org/10.1086/187509)
- Chadid, M., & Gillet, D. 1996, *A&A*, 315, 475
- Chadid, M., & Preston, G. W. 2013, *MNRAS*, 434, 552, doi: [10.1093/mnras/stt1040](https://doi.org/10.1093/mnras/stt1040)
- Chadid, M., Sneden, C., & Preston, G. W. 2017, *ApJ*, 835, 187, doi: [10.3847/1538-4357/835/2/187](https://doi.org/10.3847/1538-4357/835/2/187)
- Chadid, M., Vernin, J., & Gillet, D. 2008, *A&A*, 491, 537, doi: [10.1051/0004-6361:200810270](https://doi.org/10.1051/0004-6361:200810270)
- Chadid, M., Vernin, J., Preston, G., et al. 2014, *AJ*, 148, 88, doi: [10.1088/0004-6256/148/5/88](https://doi.org/10.1088/0004-6256/148/5/88)
- Christy, R. F. 1966, *ApJ*, 144, 108, doi: [10.1086/148593](https://doi.org/10.1086/148593)
- Fokin, A. B., & Gillet, D. 1997, *A&A*, 325, 1013
- For, B.-Q., Preston, G. W., & Sneden, C. 2011a, *ApJS*, 194, 38, doi: [10.1088/0067-0049/194/2/38](https://doi.org/10.1088/0067-0049/194/2/38)
- For, B.-Q., Sneden, C., & Preston, G. W. 2011b, *ApJS*, 197, 29, doi: [10.1088/0067-0049/197/2/29](https://doi.org/10.1088/0067-0049/197/2/29)
- Gigosos, M. A., Djurović, S., Savić, I., et al. 2014, *A&A*, 561, A135, doi: [10.1051/0004-6361/201322866](https://doi.org/10.1051/0004-6361/201322866)
- Gillet, D., & Crowe, R. A. 1988, *A&A*, 199, 242
- Gillet, D., Mauclaire, B., Lemoult, T., et al. 2019, *A&A*, 623, A109, doi: [10.1051/0004-6361/201833869](https://doi.org/10.1051/0004-6361/201833869)
- Gillet, D., Mauclaire, B., Garrel, T., et al. 2017, *A&A*, 607, A51, doi: [10.1051/0004-6361/201629897](https://doi.org/10.1051/0004-6361/201629897)
- Griem, H. R. 1983, *PhRvA*, 28, 1596, doi: [10.1103/PhysRevA.28.1596](https://doi.org/10.1103/PhysRevA.28.1596)
- Hill, S. J. 1972, *ApJ*, 178, 793, doi: [10.1086/151835](https://doi.org/10.1086/151835)
- Hodgman, S. S., Dall, R. G., Byron, L. J., et al. 2009, *PhRvL*, 103, 053002, doi: [10.1103/PhysRevLett.103.053002](https://doi.org/10.1103/PhysRevLett.103.053002)
- Kielkopf, J. F., & Allard, N. F. 2014, *Journal of Physics B Atomic Molecular Physics*, 47, 155701, doi: [10.1088/0953-4075/47/15/155701](https://doi.org/10.1088/0953-4075/47/15/155701)
- Kowalski, A. F., Allred, J. C., Uitenbroek, H., et al. 2017, *ApJ*, 837, 125, doi: [10.3847/1538-4357/aa603e](https://doi.org/10.3847/1538-4357/aa603e)
- Kramida, A., Yu. Ralchenko, Reader, J., & and NIST ASD Team. 2019, NIST Atomic Spectra Database (version 5.7.1), [Online]. Available: <https://physics.nist.gov/asd> [Aug 11 2020] National Institute of Standards and Technology, Gaithersburg, MD.
- Kukarkin, B. V. 1949 (Moscow: Government Printing Office), 182
- Kurucz, R. L. 2011, *Canadian Journal of Physics*, 89, 417, doi: [10.1139/p10-104](https://doi.org/10.1139/p10-104)
- Kurucz, R. L. 2018, in *Astronomical Society of the Pacific Conference Series*, Vol. 515, Workshop on Astrophysical Opacities, ed. C. Mendoza, S. Turck-Chi  ze, & J. Colgan, 47
- Lach, G., & Pachucki, K. 2001, *PhRvA*, 64, 042510, doi: [10.1103/PhysRevA.64.042510](https://doi.org/10.1103/PhysRevA.64.042510)
- Layden, A. C. 1994, *AJ*, 108, 1016, doi: [10.1086/117132](https://doi.org/10.1086/117132)
- Layden, A. C., Hanson, R. B., Hawley, S. L., Klemola, A. R., & Hanley, C. J. 1996, *AJ*, 112, 2110, doi: [10.1086/118167](https://doi.org/10.1086/118167)
- Marconi, M., Nordgren, T., Bono, G., Schneider, G., & Caputo, F. 2005, *ApJL*, 623, L133, doi: [10.1086/430273](https://doi.org/10.1086/430273)
- Monson, A. J., Beaton, R. L., Scowcroft, V., et al. 2017, *AJ*, 153, 96, doi: [10.3847/1538-3881/153/3/96](https://doi.org/10.3847/1538-3881/153/3/96)
- Moore, C. E. 1972, A multiplet table of astrophysical interest - Pt.1: Table of multiplets - Pt.2: Finding list of all lines in the table of multiplets, NSRDS-NBS 40 (Washington: Nat. Bur. Stds.)
- Moore, C. E., & Merrill, P. W. 1968, *Partial Grotrian Diagrams of Astrophysical Interest* (National Bureau of Standards Monograph, Washington: US Government Printing Office (USGPO))
- Moore, C. E., Minnaert, M. G. J., & Houtgast, J. 1966, *The solar spectrum 2935 A to 8770 A* (National Bureau of Standards Monograph, Washington: US Government Printing Office (USGPO))
- Neilson, H. R., Nardetto, N., Ngeow, C.-C., Fouqu  , P., & Storm, J. 2012, *A&A*, 541, A134, doi: [10.1051/0004-6361/201118550](https://doi.org/10.1051/0004-6361/201118550)
- Preston, G. W. 1959, *ApJ*, 130, 507, doi: [10.1086/146743](https://doi.org/10.1086/146743)

- . 2009, *A&A*, 507, 1621,
doi: [10.1051/0004-6361/200912984](https://doi.org/10.1051/0004-6361/200912984)
- . 2011, *AJ*, 141, 6,
doi: [10.1088/0004-6256/141/1/6](https://doi.org/10.1088/0004-6256/141/1/6)
- Preston, G. W., & Sneden, C. 2000, *AJ*, 120, 1014, doi: [10.1086/301472](https://doi.org/10.1086/301472)
- Preston, G. W., Sneden, C., Chadid, M., Thompson, I. B., & Shectman, S. A. 2019, *AJ*, 157, 153, doi: [10.3847/1538-3881/ab0ae1](https://doi.org/10.3847/1538-3881/ab0ae1)
- Prudil, Z., Dékány, I., Smolec, R., et al. 2020, *A&A*, 635, A66,
doi: [10.1051/0004-6361/201936704](https://doi.org/10.1051/0004-6361/201936704)
- Sanford, R. F. 1949, *ApJ*, 109, 208,
doi: [10.1086/145124](https://doi.org/10.1086/145124)
- Schwarzschild, M. 1952, in *Transactions IAU*, Vol. VIII, , 811
- Sneden, C., Preston, G. W., Chadid, M., & Adamów, M. 2017, *ApJ*, 848, 68,
doi: [10.3847/1538-4357/aa8b10](https://doi.org/10.3847/1538-4357/aa8b10)
- Tody, D. 1986, in *Society of Photo-Optical Instrumentation Engineers (SPIE) Conference Series*, Vol. 627, *Instrumentation in astronomy VI*, ed. D. L. Crawford, 733,
doi: [10.1117/12.968154](https://doi.org/10.1117/12.968154)
- Tody, D. 1993, in *Astronomical Society of the Pacific Conference Series*, Vol. 52, *Astronomical Data Analysis Software and Systems II*, ed. R. J. Hanisch, R. J. V. Brissenden, & J. Barnes, 173
- Unsöld, A., & Struve, O. 1949, *ApJ*, 110, 455,
doi: [10.1086/145221](https://doi.org/10.1086/145221)
- Wallerstein, G. 1959, *ApJ*, 130, 560,
doi: [10.1086/146745](https://doi.org/10.1086/146745)
- Zhang, Y., Liu, X. W., Liu, Y., & Rubin, R. H. 2005, *MNRAS*, 358, 457,
doi: [10.1111/j.1365-2966.2005.08810.x](https://doi.org/10.1111/j.1365-2966.2005.08810.x)
- Zinn, R. 1985, *ApJ*, 293, 424, doi: [10.1086/163249](https://doi.org/10.1086/163249)

Table 1. Program Star Data

Name	P	T_0	V	V_{amp}	[Fe/H]
	(d)	(d)	(mag)	(mag)	
WY Ant	0.574340	1870.76	10.37	0.85	-1.80
X Ari	0.651172	1890.10	9.24	0.94	-2.60
RR Cet	0.553030	2143.63	9.26	0.82	-1.56
W Crt	0.412011	1871.64	10.90	1.10	-0.59
DX Del	0.472650	2415.85	9.81	0.70	-0.44
DT Hya	0.567970	1872.11	12.53	0.98	-1.39
SS Leo	0.626330	1873.06	10.47	1.00	-1.88
ST Leo	0.477983	2384.94	10.99	1.19	-1.30
RV Oct	0.571184	1891.66	10.53	1.13	-1.46
V445 Oph	0.397030	1939.03	10.54	0.81	-0.10
AV Peg	0.390385	2758.11	9.95	0.96	-0.13
HH Pup	0.390745	1869.65	10.57	1.24	-0.74
AN Ser	0.522080	2701.17	10.46	1.01	+0.04
W Tuc	0.642260	1869.52	10.90	1.11	-1.76
UU Vir	0.475597	1886.54	10.06	1.08	-0.92

Table 2. Phase Shifts and Flux Scale factors

Quantity	RR Cet	RV Oct	SS Leo	ST Leo	W Tuc	WY Ant	X Ari
flux scale factors							
H α	1.136	1.085	0.910	1.450	1.104	1.040	0.770
He I 5876 Å	1.135	0.850	0.780	1.200	1.640	1.020	1.000
phase shifts $\Delta\phi$							
H α	0.0060	-0.0095	-0.0035	-0.0220	-0.0035	0.0090	0.0061
He I 5876 Å	0.0080	-0.0050	-0.0005	-0.0180	0.0005	0.0085	0.0053

Table 3. Kinematic Properties of RRab Stars During Primary Light Rise ^a

Star	dR/Dt	dR/dt	dR/dt	σ_{Max}	σ_{Max}	σ_{Max}
	H α (B)	H α (R)	H α (B-R)	H α (B)	H α (R)	H α (B-R)
RR Cet	86.4	-71.6	158.0	85.8	57.8	28.0
RV Oct	93.6	-72.1	165.7	81.7	57.8	23.9
SS Leo	87.5	-76.2	163.7	83.2	59.1	24.1
W Tuc	109.9	-71.9	181.8	94.0	72.3	21.7
WY Ant	87.9	-73.3	161.2	87.3	64.8	22.5
X Ari	88.4	-74.2	162.6	87.8	60.1	27.7
mean	92.3	-73.2	165.5	86.6	62.0	24.7
σ	8.2	1.6	7.7	3.9	5.2	2.4
	He I	He I	He I	He I	He I	He I
RR Cet	57.8	-87.7	145.5	43.8	28.6	15.2
RV Oct	58.0	-73.8	131.8	39.8	23.3	16.5
SS Leo	53.0	-73.5	126.5	40.6	26.5	14.1
W Tuc	52.2	-69.6	121.8	45.2	36.1	9.1
WY Ant	48.2	-74.6	122.8	39.6	39.3	0.3
X Ari	53.1	-62.9	116.0	51.6	43.3	8.3
mean	53.7	-73.7	127.4	43.4	32.9	10.6
σ	3.4	7.4	9.4	4.2	7.2	5.5

^aQuantities measured at phase $\phi \simeq 0.97$

Table 4. Regression constants for dR/dt and σ_{Max}

Star	feature	dR/Dt(B)		dR/dt(B)		dR/dt(R)		σ_{Max} (B)		σ_{Max} (R)	
		a0	a1	a0	a1	a0	a1	a0	a1	a0	a1
RR Cet	H α	186.554	-103.250	523.387	-613.388	-204.589	299.338	258.439	-206.717		
RV Oct	H α	-34.041	131.576	249.885	-331.951	-72.621	159.074	201.159	-147.791		
SS Leo	H α	-216.277	313.160	614.894	-709.663	-249.830	343.312	272.169	-219.620		
W Tuc	H α	12.285	100.665	134.548	-212.862	56.774	38.419	93.955	-22.313		
WY Ant	H α	59.292	31.410	283.985	-368.308	-76.043	168.379	258.183	-199.415		
X Ari	H α	-146.453	242.098	137.306	-218.010	35.781	53.628	326.617	-274.785		
RR Cet	He I	-850.430	936.342	572.532	-680.664	-78.794	126.436	-217.945	254.132		
RV Oct	He I	-1020.236	1111.608	313.749	-399.558	84.620	-46.234	-32.516	57.567		
SS Leo	He I	-865.432	946.876	614.894	-709.663	-124.863	170.547	-6.733	35.940		
W Tuc	He I	-809.648	888.546	360.180	-443.044	-148.486	199.692	-96.769	136.933		
WY Ant	He I	-689.407	760.464	464.721	-556.043	-107.779	151.970	-202.714	249.459		
X Ari	He I	-781.674	860.612	437.561	-515.920	<i>a</i>	<i>a</i>	<i>b</i>	<i>b</i>		

^aQuadratic fit: $\sigma_{Max} = -8531 + 17733\phi - 9160\phi^2$

^bQuadratic fit: $\sigma_{Max} = -10910 + 22426\phi - 11478\phi^2$